# A biomimetic red blood cell inspired encapsulation design for advanced hydrate-based carbon capture

Zhang, Yuxuan; Zhai, Xiaoqiang; Zhang, Fengyuan; Zhang, Zhongbin; Hooman, Kamel; Zhang, Hai; Wang, Xiaolin

**Important note**
To cite this publication, please use the final published version (if applicable).
Please check the document version above.

# A biomimetic red blood cell inspired encapsulation design for advanced hydrate-based carbon capture

Yuxuan Zhang [a], Xiaoqiang Zhai [b], Fengyuan Zhang [a], Zhongbin Zhang [c], Kamel Hooman [d], Hai Zhang [e], Xiaolin Wang [a,*]

[a] *School of Engineering, The Australian National University, Canberra, ACT, 2601, Australia*
[b] *Institute of Refrigeration and Cryogenics, Shanghai Jiao Tong University, Shanghai, 200240, China*
[c] *School of Energy and Mechanical Engineering, Nanjing Normal University, Nanjing, Jiangsu, 210046, China*
[d] *Department of Process and Energy, Delft University of Technology, Leeghwaterstraat 39, 2628CB, Delft, The Netherlands*
[e] *Institute of Thermal Energy Engineering, Shanghai Jiao Tong University, Shanghai, 200240, China*

## ARTICLE INFO

## ABSTRACT

Enhancing gas-liquid mass transfer is key to promote gas hydrate formation kinetics. Encapsulation of $CO_2$ hydrate is expected to dramatically increase gas-liquid contact to enhance mass transfer. However, gas hydrate encapsulation has never been proposed as the technical issues of gas permeation through capsule shells have never been addressed. In this work, based on the principles of biomimetics, we proposed a novel red blood cell (RBC) inspired carbon capture capsule to promote $CO_2$ hydrate formation kinetics. An experimentally validated model is established to compare the carbon capture performance in an RBC-shaped and a spherical capsule. It is revealed that the gas uptake efficiency of the RBC-shaped capsule is 143% higher than that of the spherical one. The effect of initial pressure and capsule size on $CO_2$ hydrate formation kinetics is also investigated. Furthermore, the structure of RBC is optimised and it is found the average amount of hydrate formation per surface area achieves a peak when the ratio of the height at the centre to the width of the ring is between 0.128 and 0.160, which is close to that of real RBCs in human bodies. This work enables the informed design of hydrate-based carbon capture units with high gas uptake efficiency.

## 1. Introduction

$CO_2$ hydrate is a safe, clean and cost-effective material which makes use of the ability of gas hydrates to selectively store $CO_2$ molecules to remove $CO_2$ gas from emitted gas mixtures, i.e. hydrate-based carbon capture (HBCC) [1]. It is formed under certain conditions, called phase equilibrium, usually under high pressure and low temperature [2]. During the formation, $CO_2$ molecules are trapped into hydrogen bonded cages of water molecules to formulate a stable crystal structure [3]. When the temperature-pressure condition departs from phase equilibrium, $CO_2$ hydrate dissociates and $CO_2$ molecules are released. The formation of $CO_2$ hydrate is exothermic and the dissociation of $CO_2$ hydrate is endothermic [4]. $CO_2$ hydrate technology has great potential in the field of emission control for its high reversibility and large storage capacity [5].

The phase equilibrium pressure of $CO_2$ hydrate is significantly high, which can be up to 4 MPa corresponding to a phase equilibrium temperature of 8 °C. However, it can be reduced to the safe working pressure range by using chemical thermodynamics promoters such as tetra-*n*-butylammonium bromide (TBAB) [6–8], tetrahydrofuran (THF) [9], tetra-*n*-butylammonium fluoride (TBAF) and tetra-*n*-butylammonium chloride (TBAC) [10,11], tetra-*n*-butylphosphonium bromide (TBPB) [12], etc. TBAB is the most intensively studied additive to modify the phase equilibrium conditions of $CO_2$ hydrate. Generally, TBAB can decrease the formation pressure by a fact of 10–50 [13]. Currently, the main obstacle restricting the wide application of $CO_2$ hydrate is the low gas uptake at low driving force [14], which is mainly caused by the low contact area between gas and liquid and the blockage on the gas-liquid interface resulting from formed hydrates [15,16]. It was found the $CO_2$ uptake is only 15.4% of the rate capacity at 5.5 bar in 5.3 h [4], which causes a large amount of un-reacted water trapped between hydrate particles and increases the capital and operational cost [17].

Enhancing the gas-liquid mass transfer is a promising method in improving $CO_2$ uptake in gas hydrates. Various strategies have been

---

## Nomenclature

| | |
|---|---|
| $n$ | number of moles (mol) |
| $P$ | pressure (Pa) |
| $V$ | volume (m$^3$) |
| $R$ | ideal gas constant (J mol$^{-1}$ K$^{-1}$) |
| $T$ | temperature (K) |
| $Z$ | compressibility factor |
| $x$ | solubility |
| $c$ | concentration (mol m$^{-3}$) |
| $t$ | time (s) |
| $D_e$ | effective diffusivity (m$^2$ s$^{-1}$) |
| $D_0$ | pre-exponential factor of diffusion coefficient (m$^2$ s$^{-1}$) |
| $K$ | reaction rate constant (m$^3$ mol$^{-1}$ s$^{-1}$) |
| $k$ | thermal conductivity (W m$^{-1}$ K$^{-1}$) |
| $Q$ | enthalpy (J) |
| $c_0$ | initial concentration of TBAB (mol m$^{-3}$) |
| $n_{95}$ | 95% of the maximum amount of hydrate (mol) |
| $t_{95}$ | time required when the amount of hydrate reaches $n_{95}$ |

| | |
|---|---|
| | (min) |
| $J$ | diffusion flux (mol m$^{-2}$ s$^{-1}$) |
| $d$ | thickness (m) |

*Greek symbols*

| | |
|---|---|
| $\rho$ | density (kg m$^{-3}$) |
| $\varepsilon$ | reduction factor (m$^3$ K mol$^{-1}$) |

*Subscripts*

| | |
|---|---|
| ini | initial state |
| eq | equilibrium state |
| sol | solution |
| hyd | hydrate |
| diss | dissolved |
| g | gas |
| u | upside |
| d | downside |
| m | membrane |
| exp | experiment |
| sim | simulation |

proposed to enhance mass transfer in hydrate formation, including adding surfactants [18–20], enhanced mechanical mixing by stirring [21], injecting [22] or bubbling [23], and the use of porous media such as hydrophilic silica gels [24,25], silica sands [26], white corundum [27], active carbon [28] or metal skeleton [29,30]. However, technical difficulties exist when applying these solutions. For instance, the effect of surfactants varies with the initial concentration and type [31]. Besides, the synergic effects are uncertain when more than one surfactant is added. The enhanced mechanical mixing always incurs extra energy consumption and impairs the system stability. Although porous media can significantly enhance the contact area between gas and liquid, it may have problems in recyclability and stability [14,32].

Another potential strategy to improve gas-liquid mass transfer that has not been proposed is to use biomimetic encapsulation. Red blood cell (RBC) is a common type of blood cell in vertebrates and its primary function is to deliver oxygen to body tissues and transport $CO_2$ to lungs. After countless generations of evolution, RBC has formed a unique biconcave disc-shaped structure, which allows for a high surface-area-to-volume ratio to facilitate gas diffusion and mass transfer. It is believed that the RBC-shaped encapsulation is favourable to enhance gas uptake to form gas hydrates. In the past few years, the RBC-shaped phase change material (PCM) capsules have been proposed and their excellent heat transfer performance has been validated [33–35]. It was found that the heat transfer rate of RBC-shaped PCM capsule was about two times higher than the spherical capsule with the same volume [33]. However, no research has been conducted on the gas-liquid mass transfer enhancement to form gas hydrates by using RBC-shaped encapsulation, which will be the main focus of this research.

The concept of RBC inspired encapsulation design and its potential application in HBCC system are illustrated in Fig. 1 (a)-(b). In a conventional hydrate formation reactor, gas uptake efficiency is severely limited by the low gas-liquid interface area. However, through the design philosophy of encapsulation, the bulk liquid phase can be separated into a number of scattered capsules, and the interface area between gas and liquid is dramatically increased (as shown in Fig. 1 (a)), which will consequently greatly improve gas uptake efficiency. The mechanism of $CO_2$ transport in the capsules is similar to that of gas transport in real human RBCs. Fig. 1 (b) shows one type of potential applications of RBC inspired encapsulation in HBCC system. In this scenario, flue gas enters the HBCC unit at appropriate conditions to form $CO_2$ hydrate in the capsules. In this process, cooling capacity is stored and $CO_2$-lean gas is produced and exits the tank. For the capsules in which hydrates have been formed, dissociation process can be trigered
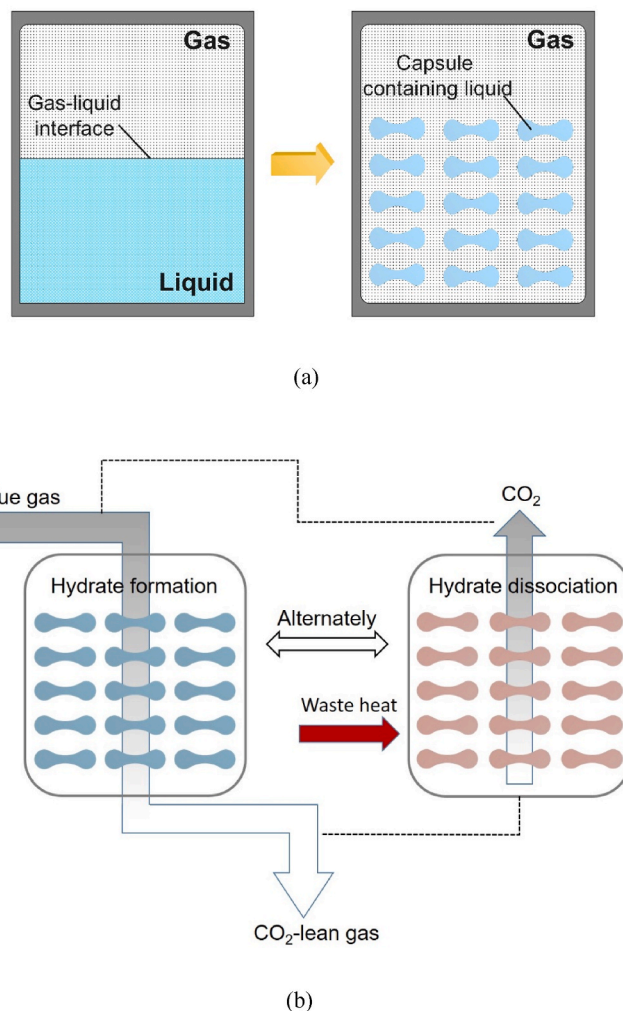


(a)



(b)

**Fig. 1.** (a) Comparison between conventional and RBC inspired encapsulation HBCC reactor, (b) a schematic of the application of RBC inspired encapsulation in a HBCC system.

by recycling industrial waste heat, and $CO_2$ is therefore released. The process if fully reversible. It can be operated by one unit periodically or two units alternatively. In this way, the RBC inspired encapsulation design can contribute to tackle with current challenges in energy storage and greenhouse gas emissions in an efficient and economic way with acceralbrated $CO_2$ charge and discharge.

Generally, kinetic models of gas hydrate formation are structured based on different controlling mechanisms including mass transfer, heat transfer and intrinsic reaction kinetics [36]. In the past decades, a considerable number of kinetic models of hydrate growth have been developed for the conditions in laboratory-scale stirred tank reactors. The driving force defined in these studies include fugacity difference [37–39], chemical potential difference [40–42] or concentration difference [43,44] between the guest gas dissolved in the solution and in the phase equilibrium condition. These models have been widely used, however, it is argued that most of them are likely to be apparatus-dependent [36]. In some research works, kinetic model of gas hydrate formation is also developed from the perspective of chemical reaction. Yang et al. [45] investigated the kinetics of $CO_2$ hydrate formation in a tubular reactor and applied a first-order reaction rate law to represent the global rate of hydrate formation. Under vigorous inter-phase mixing and high gas volume fractions conditions, mass transfer resistance is significantly reduced, and the hydrate formation kinetics can be fit well to the first order model.

Under conditions without sufficient mixing among different phases, the mass transfer resistance for the diffusion of dissolved gas from the bulk solution to the hydrate-liquid interface cannot be neglected and, therefore, the diffusion term needs to be taken into account in the kinetic models. Shindo et al. [46] developed a diffusion-reaction model for the formation of $CO_2$ hydrate at the interface between liquid $CO_2$ and water. Mass balance equations of hydrate and water considering both molecular diffusion and intrinsic reaction were formulated and solved with numerical methods. The predicted hydrate film thickness by this model is in good agreement with the findings about $CO_2$ hydrate formation [47]. The diffusion-reaction model of Shindo et al. were further modified and improved in many other studies concerning gas hydrate formation kinetics [48–50]. However, a major shortcoming of the existing diffusion-reaction models is that the diffusion coefficient incorporated into the diffusion equation is assumed to be a constant. In fact, with the growth of gas hydrate, the thickness of hydrate film grows, and the overall mass transfer efficiency should descend since the hydrate film becomes a significant barrier for mass transfer between gas and water [51,52]. Therefore, it can be inferred that the diffusion coefficient should be a function of the concentration of formed hydrate in the system.

In this paper, the effects of RBC inspired encapsulation design on $CO_2$ hydrate formation kinetics will be investigated. Firstly, an appropriate hydrophobic and breathable membrane is selected to retain liquid inside and allow gas to penetrate, and an RBC-shaped skeleton is designed and produced to serve as a support for the membrane. A spherical skeleton is also produced for comparison. An experimentally validated diffusion-reaction kinetic model is proposed to explore the mass and heat transfer process inside the RBC-shaped and spherical capsules. The effects of initial pressure and capsule size on the gas hydrate formation kinetics are investigated using the numerical model. Finally, the RBC structure is optimised through numerical simulation in order to achieve best $CO_2$ uptake performance.

## 2. Methods

### 2.1. Experimental methods and procedures

#### 2.1.1. Preparation of capsules

Based on the natural structure of human RBC, the key structural parameters can be extracted to form a simplified geometrical model, and the schematic of the rotational symmetry plane of RBC is shown in Fig. 2.
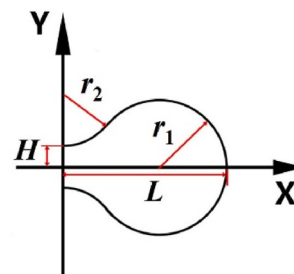


**Fig. 2.** Schematic of the rotational symmetry plane of RBC.

$H$ stands for the height at the centre, $r_2$ stands for radius of the arc at the centre, and $L$ and $r_1$ stand for the width and radius of the RBC ring, respectively.

The relationship between the four parameters of $H$, $L$, $r_1$ and $r_2$ can be expressed as:

$$(H + r_2)^2 + (L - r_1)^2 = (r_1 + r_2)^2 \tag{1}$$

In this work, the values of $H$, $L$, $r_1$ and $r_2$ are set as 3.080, 24.53, 7.798 and 24.22 mm, respectively.

Red blood cell membrane serves as a vital part to maintain the structure and contain the contents of the RBC, and it also plays a critical role in maintaining cellular functions like nutrients and gas transport. The native red blood cell membranes have a cytoskeleton meshwork to support the structural stability and elasticity of the membranes [53]. Inspired by the natural structure of RBC, we selected a hydrophobic and breathable membrane that can retain liquid inside and allow gas to penetrate. We designed an RBC-shaped skeleton to support and stabilise the RBC structure, as shown in Fig. 3 (a), and a spherical skeleton for comparison, as shown in Fig. 3 (b). Both the two capsules have the same internal volume of 22.5 mL.
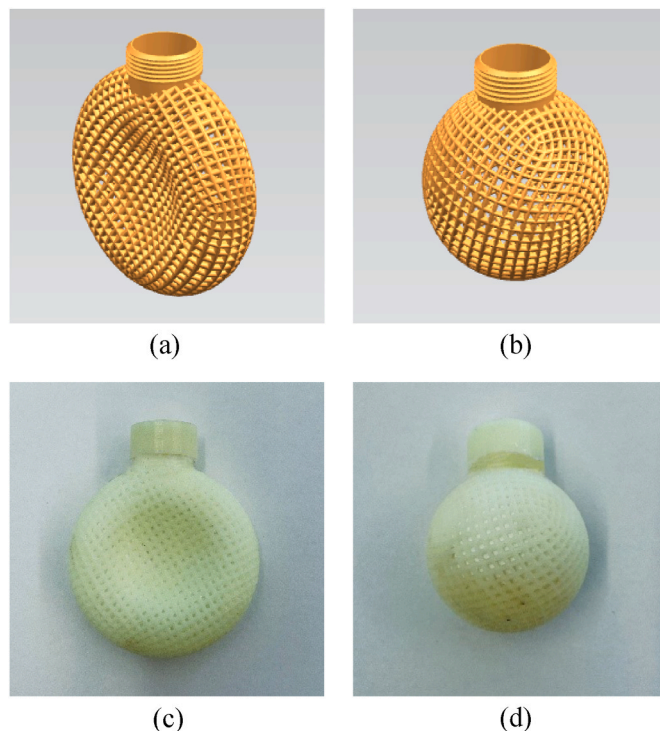


**Fig. 3.** Models of the skeletons and 3D printed capsules with membrane: (a) the 3D model of RBC capsule, (b) the 3D model of spherical capsule, (c) the appearance of 3D-printed RBC capsule with hydrophobic and breathable membrane, and (d) the appearance of 3D-printed spherical capsule with hydrophobic and breathable membrane.

The membrane is made of porous poly (tetrafluoroethylene) (PTFE), which is characterised by strong hydrophobicity, good breathability, high heat resistance and outstanding chemical stability [54]. The thickness of the membrane is about 15 μm. The skeletons are produced through 3D printing using high toughness resin as the material. The 32-wt% TBAB solution is used as the medium to absorb $CO_2$ and form hydrates. The pictures of 3D-printed capsules with hydrophobic and breathable membrane containing the solution are shown in Fig. 3 (c) (d), and the main thermal properties of the membrane, skeleton and solution are shown in Table 1.

### 2.1.2. Experimental setup

The experimental apparatus is shown in Fig. 4. It consists of a cylindrical reactor with an internal volume of 556 mL, a thermostatic bath with an internal volume of 30 L, a $CO_2$ gas cylinder and a data acquisition system. The $CO_2$ gas cylinder with the purity greater than 99.9% was supplied by BOC Ltd. Australia. The thermostatic bath used 30-vol% propylene glycol as the cooling fluid with a freezing point of $-13.3\,°C$. A pressure sensor was used to record the pressure in the reactor and two thermocouples were attached to the upper and lower parts of the reactor respectively to record the temperature in the reactor. The average temperature recorded by the thermocouples was regarded as the average temperature in the reactor. The accuracies of the pressure sensor and the thermocouples are 0.25% and 0.75%, respectively. The results were logged every 10 s by the data acquisition system. The air tightness of the experimental apparatus was examined to ensure there was no gas leakage during the experiment.

The experiment was conducted at a constant temperature of 12 °C under the pressure of 4 MPa (initial pressure) in a closed system. Before the experiment, the thermostatic bath was turned on and set at 12 °C. When it was stable at the target temperature, the capsule was placed into the reactor and the reactor was closed tightly. Then the reactor was purged with $CO_2$ and vented for three times to remove the residual air. Then $CO_2$ was slowly charged into the reactor to the target pressure to trigger the gas hydrate formation. The experiment was terminated when pressure remained stable for an hour to ensure the full completion of hydrate formation and no liquid solution remaining. The experiment was repeated twice for both the RBC-shaped and spherical capsules. The possible errors of the experiment mainly come from the measurement error of the pressure sensor and thermocouples.

### 2.1.3. Calculation of the amount of hydrate

At the end of hydrate formation, the amount of $CO_2$ in the solution can be obtained by:

$$n_{CO_2,sol} = n_{ini} - n_{eq} = \frac{P_{ini}V_g}{Z_{ini}RT} - \frac{P_{eq}V_g}{Z_{eq}RT} \quad (2)$$

where $P$ is the pressure, $V$ is the volume of gas, $R$ is the ideal gas constant, $T$ is the temperature, and $Z$ is the gas compressibility factor.

$n_{CO_2,sol}$ equals the total amount of $CO_2$ in the hydrate and dissolved in the solution:

$$n_{CO_2,sol} = n_{CO_2,hyd} + n_{CO_2,diss} \quad (3)$$

The amount of $CO_2$ dissolved in the solution can be calculated by:

$$n_{CO_2,diss} = \frac{x_{CO_2}}{1 - x_{CO_2}} \left( n_{TBAB,sol} + n_{water,sol} \right) \quad (4)$$

where $x_{CO_2}$ is the solubility of $CO_2$ in the TBAB solution, which can be estimated based on the experimental results in the literature [60].

Based on a previous study [13], the composition of hydrate is determined as $2.49CO_2 \cdot TBAB \cdot 38H_2O$, then the amount of hydrate can be calculated as $n_{CO_2,hyd}/2.49$.

### 2.2. Modelling

The hydrate growth mechanism can be regarded as a combination of three different factors: (1) mass transfer of gas molecules to the hydrate surface; (2) intrinsic kinetics of hydrate formation at the hydrate surface; (3) heat transfer from the exothermic hydrate formation reaction [36]. In this work, we developed a macro-scale numerical model considering the effects of mass transfer, heat transfer and intrinsic kinetics in order to investigate the performance and influencing factors of the hydrate formation kinetics in a capsule. As both the reactor and the capsules are axisymmetric, the model can be simplified and developed in a 2D approach, and a schematic of the model is shown in Fig. 5. Both the reactor and capsule are taken as the computational domain. Some assumptions are made for the model: (1) the initial temperature and concentration distribution in the reactor are uniform; (2) the thermos-physical properties of the hydrate-solution mixture change linearly with the mole fraction of hydrate; (3) the solubility of $CO_2$ in the TBAB solution follows Henry's law; and (4) convection inside the capsules can be neglected.

### 2.2.1. Governing equations

The mass transfer equations considering the intrinsic reaction are:

$$\frac{\partial c_g}{\partial t} = D_e \nabla^2 c_g - nKc_g \left( c_0 - c_{hyd} \right) \quad (5)$$

$$\frac{\partial c_{hyd}}{\partial t} = Kc_g \left( c_0 - c_{hyd} \right) \quad (6)$$

where $c_g$ and $c_{hyd}$ represent the concentration of $CO_2$ and hydrate, respectively. $c_0$ is the initial concentration of TBAB, which is 1048 mol $m^{-3}$ for 32-wt% TBAB solution. $n$ is the stoichiometric number of $CO_2$ in the composition of hydrate, which is taken as 2.49 in this work. $K$ is the reaction rate constant and $D_e$ is the effective diffusivity of $CO_2$ in the capsule, which can reflect the influence of hydrate formation on the diffusivity of $CO_2$. $D_e$ should decrease with the growth of gas hydrate since the hydrate film could be a significant barrier for mass transfer [51, 61]. In this work, we used an Arrhenius type of equation to describe the variation of effective diffusivity, which is given by:

$$D_e = D_0 e^{-\frac{\varepsilon \times c_{hyd}}{T}} \quad (7)$$

where $D_0$ is the pre-exponential factor of diffusion coefficient, $c_{hyd}$ is the concentration of hydrate in the capsule, $T$ is temperature and $\varepsilon$ is the reduction factor.

Hydrate formation is an exothermic process and will lead to temperature gradient in the capsule. A heat transfer model is coupled with the diffusion-reaction model to predict the temperature profile in the capsule. Since convection and radiation are negligible, conduction will be the only heat transfer mode in the capsule, and the governing equations can be written as:

$$\rho C_p \frac{\partial T}{\partial t} + \nabla \cdot \mathbf{q} = Q \quad (8)$$

$$\mathbf{q} = -k\nabla T \quad (9)$$

where $\rho$ is density, $C_p$ is heat capacity, $T$ is temperature, $k$ is thermal conductivity, and $Q$ is the hydrate formation enthalpy, which is taken as $-318.5$ kJ/kg measured by the T-history method [13]. The values of the thermos-physical properties of both the solution and hydrate are listed
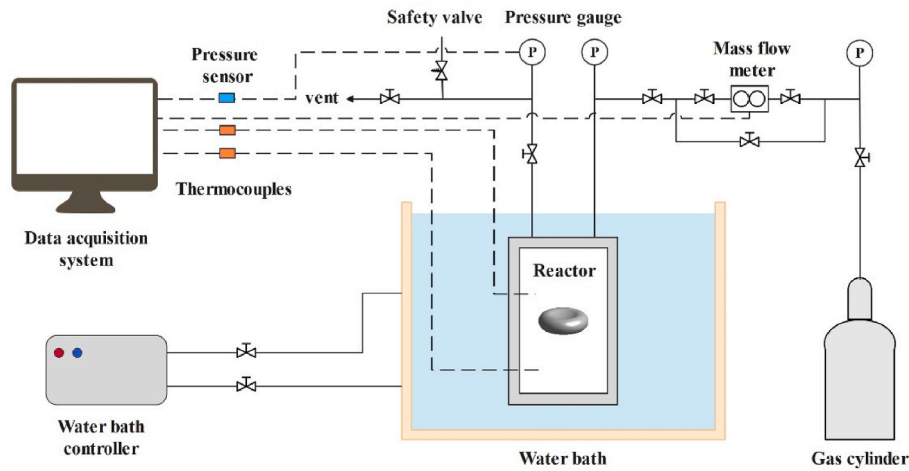
**Table 1**
Main thermal properties of the materials and the solution.

| | Density (kg m$^{-3}$) [55,56] | Thermal conductivity (W m$^{-1}$ K$^{-1}$) [55,57] | Heat capacity (J kg$^{-1}$ K$^{-1}$) [58,59] |
|---|---|---|---|
| Membrane | 2240–2330 | 0.440–0.764 | 970–1090 |
| Skeleton | 1010–1210 | 0.150–0.200 | 1390–1920 |
| Solution | 1030–1082 | 0.339–0.351 | 3600–3800 |

**Fig. 4.** Schematic diagram of the experimental setup.
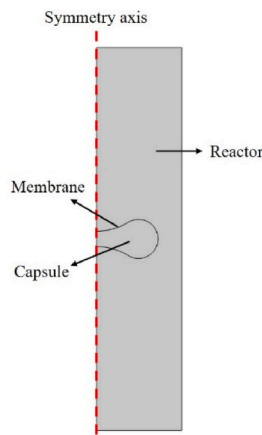


**Fig. 5.** Schematic of the numerical model.

**Table 2**
Thermos-physical properties of the solution and hydrate.

|  | $\rho$ (kg m$^{-3}$) | $C_p$ (J kg$^{-1}$ K$^{-1}$) | $k$ (W m$^{-1}$ K$^{-1}$) |
|---|---|---|---|
| Solution | 1056 | 3700 | 0.339 |
| Hydrate | 1090 | 2480 | 0.380 |

in Table 2 [57,62].

### 2.2.2. Initial and boundary conditions

For the membrane side, a continuity condition is applied:

$$-\mathbf{n} \cdot \mathbf{J}_{i,u} = \frac{D_{m,i}}{d_m} \left( c_{i,d} - c_{i,u} \right) \tag{10}$$

$$-\mathbf{n} \cdot \mathbf{J}_{i,d} = \frac{D_{m,i}}{d_m} \left( c_{i,u} - c_{i,d} \right) \tag{11}$$

where $\mathbf{J}_{i,u}$ and $\mathbf{J}_{i,d}$ represent the diffusion flux of the upside and downside of element $i$, $c_{i,u}$ and $c_{i,d}$ represent the concentration of the upside and downside of element $i$, respectively. $d_m$ is the thickness of the membrane, and $D_m$ is the diffusivity of $CO_2$ in the membrane, which can be fitted with an Arrhenius-type equation reported by Sebők et al. [63].

For the boundaries of the reactor, no flux condition is applied:

$$-\mathbf{n} \cdot \mathbf{J}_i = 0 \tag{12}$$

For the boundaries of the capsule, constant temperature condition is applied:

$$T = T_s \tag{13}$$

$T_s$ is set to 286.3 K, as measured by the thermocouples.

The axisymmetric boundary condition is applied to the symmetry axis of the reactor and capsule as depicted by the red dotted line in Fig. 5.

The initial conditions of $CO_2$ in the reactor are defined as follows:

$$p = p_0, T = T_0 \tag{14}$$

where $p_0$ and $T_0$ are set to 4 MPa and 288.9 K, according to the experimental conditions.

The least-squares objective is employed for the simulation and experiment results. $D_0$, $K$, and $\varepsilon$ are optimised by curve fitting and the optimal parameters of the model are obtained using the levenberg-marquardt algorithm [64]. To assess the accuracy of the model, the mean relative difference (MRD) between the experiment and simulation results is calculated by

$$MRD = \frac{1}{N} \times \frac{\sum \left| x_{i,sim} - x_{i,exp} \right|}{x_{i,exp}} \times 100\% \tag{15}$$

where $N$ represents the number of data points.

### 2.2.3. Mesh and time step independency study

Triangular mesh was generated for the numerical models. At the boundaries of the capsule, mesh was refined to better capture gradients. Prior to the validation, independency study of mesh and time step size was conducted. The variation of the amount of hydrate (mol) over time for the model of RBC-shaped capsule with different number of cells and time step sizes is plotted and shown in Fig. 6. The time step size is 1 min in Fig. 6 (a) and the number of cells is $5.4 \times 10^4$ in Fig. 6 (b). It is shown that the result is independent of the cell number when it is close to or higher than $5.4 \times 10^4$, and when the cell number is fixed at $5.4 \times 10^4$, the effect of time step size is negligible when it is lower than 1 min. Therefore, the cell number of $5.4 \times 10^4$ and the time step size of 1 min were selected for the simulations in the RBC-shaped and spherical models.

## 3. Results and discussion

### 3.1. Experiment results and model validation

The pressure and temperature profiles of both the spherical and RBC-shaped capsules during $CO_2$ hydrate formation are shown in Fig. 7. For
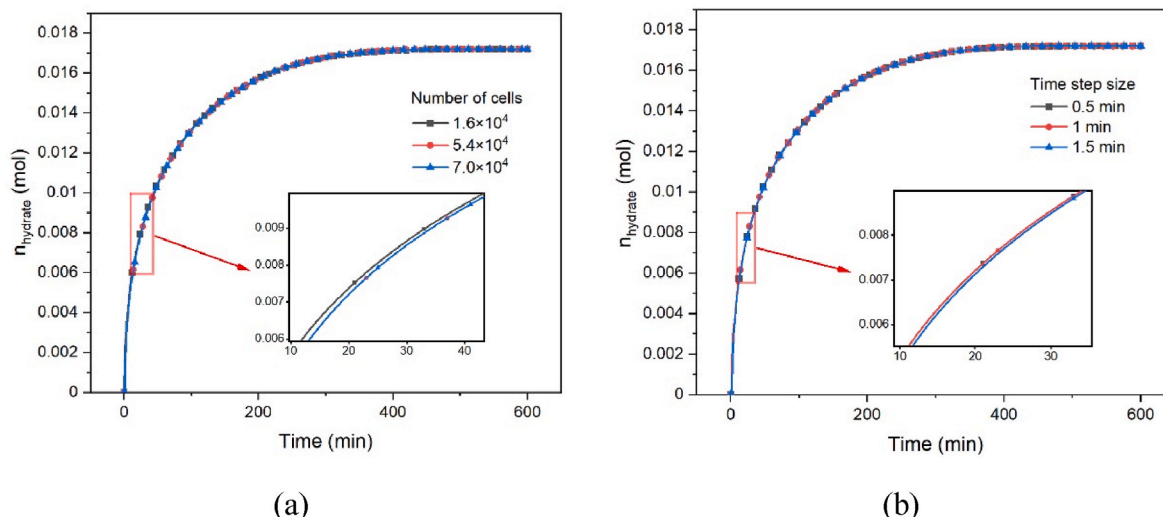
**Fig. 6.** The variation of the amount of hydrate over time for the RBC-shaped capsule with (a) different mesh cell numbers and (b) different time step sizes.
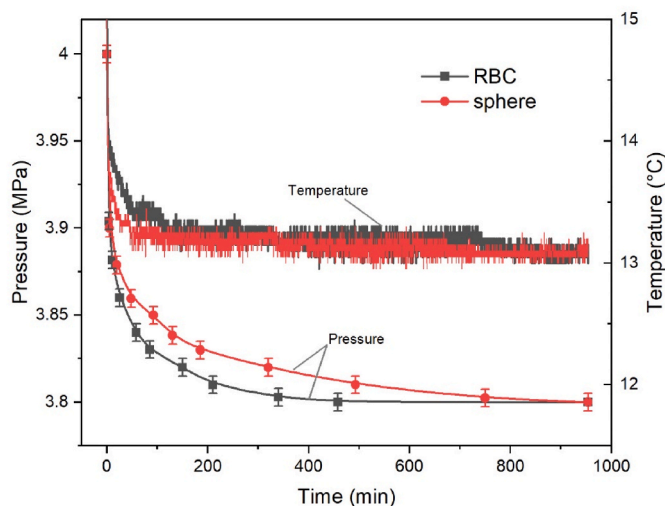


**Fig. 7.** Pressure variation over time for the RBC-shaped and spherical capsules.

both capsules, pressure drops rapidly in the early stage of hydrate formation, and then the dropping trend slows down. The phenomenon is mainly caused by two reasons. Firstly, the temperature of the injected gas is higher than the temperature in the reactor, the injected gas is cooled and pressure drops rapidly in the early stage (as evidenced by the temperature profile). Secondly, the contact area between gas and liquid is larger and the gas diffusion resistance is lower in the early stage. With the growth of hydrate layer, the contact area decreases and diffusion resistance increases, therefore the decreasing trend of pressure slows down. Although hydrate formation is exothermic, the temperature in the reactor is almost stable in the later stage due to the constant temperature in the water tank. It can be noted that pressure drops more rapidly for the RBC-shaped capsule. The pressure is almost stable at about 400 min for the RBC-shaped capsule, indicating the hydrate formation reaction is complete; while it takes about 900 min for the pressure to be flat for the spherical capsule. Based on the pressure variations, the amount of formed hydrate (mol) during the formation can be calculated and fitted with the simulation results. Fig. 8 (a) and (b) show the validation results for the RBC-shaped and spherical capsule, respectively. A good agreement has been achieved between the simulation results and experiment data. The value of MRD is 2.01% for the RBC-shaped capsule, and 2.56% for the spherical capsule. The optimised parameters in the model are
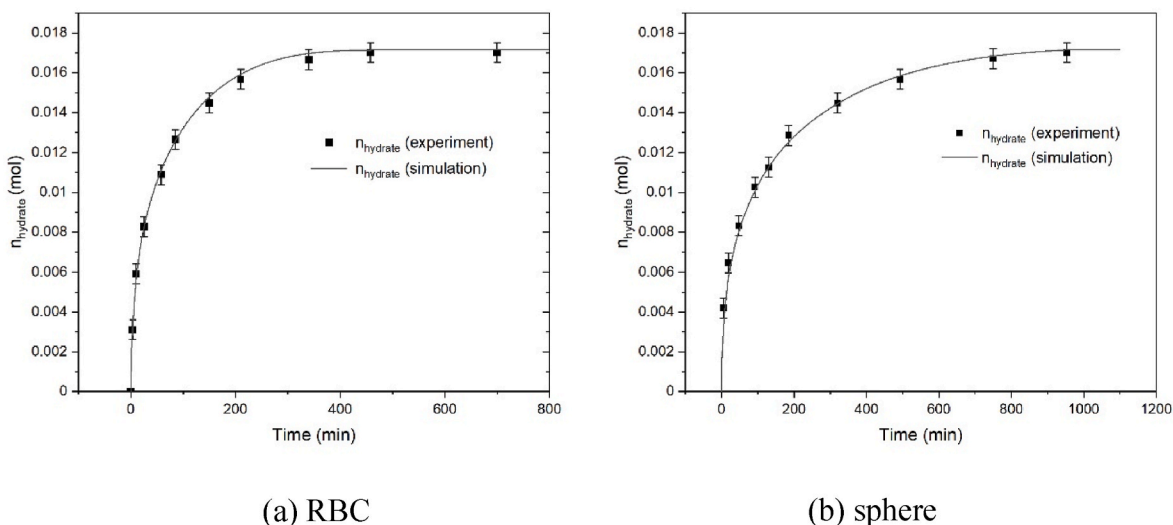


(a) RBC

(b) sphere

**Fig. 8.** Validation for RBC-shaped and spherical capsules.

**Table 3**
Summary of optimal parameters in the numerical model.

| Parameters | $D_0$ ($\times 10^{-9}$ m$^2$ s$^{-1}$) | $K$ ($\times 10^{-4}$ m$^3$ mol$^{-1}$ s$^{-1}$) | $\varepsilon$ (m$^3$ K mol$^{-1}$) |
|---|---|---|---|
| Optimised value | 2.2328 | 5.3480 | 0.9655 |

listed in Table 3.

It can be found in Fig. 8 that during the hydrate formation process, the formation rate keeps decreasing due to the blocking on the gas-water interface resulting from formed hydrates. As hydrate grows, the blocking effect becomes more significant, and thus the effective diffusivity of $CO_2$ decreases. Fig. 9 shows the variation of effective diffusivity and the dropping rate of effective diffusivity at the initial stage and later stage during hydrate formation process for both capsules. The effective diffusivity drops about ten times as the hydrate grows. At the initial stage, the dropping rate of effective diffusivity for the RBC-shaped capsule is higher than that of the spherical capsule, since the RBC shape has a larger surface-to-volume ratio than the sphere, resulting in a larger gas-water interface area for hydrate formation at the initial stage. Therefore, compared to the spherical capsule, RBC has a faster growth of hydrate layer within the same time, which leads to a lower effective diffusivity. At the later stage, the concentration of hydrate in the RBC-shaped capsule is much higher than the spherical capsule, resulting in a lower hydrate growth rate and thus lower dropping rate of effective diffusivity for the RBC-shaped capsule. Fig. 10 shows a schematic of the diffusion resistance (defined as thickness divided by diffusivity) of different parts of a RBC-shaped capsule during the hydrate formation process. As hydrate grows inward, the diffusion resistance of the hydrate film increases and becomes much higher than that of the hydrophobic membrane and liquid. Encapsulation of hydrate can greatly shorten the diffusion distance through the hydrate film, and therefore improve gas uptake efficiency. Compared to the spherical one, the RBC-shaped capsule has lower diffusion resistance due to its structural features.

In engineering applications, it is not cost-effective to achieve a maximum gas uptake capacity, since a minor increase in the gas uptake will take much longer time in the later stage of the reaction. In this work, we compared the reaction time ($t_{95}$) when it reaches 95% of the maximum amount of hydrate ($n_{95}$) for the RBC-shaped and spherical capsules, with the results shown in Fig. 11. For the spherical capsule, $t_{95}$ is 580 min, while for the RBC-shaped capsule, it reduces to 239 min,
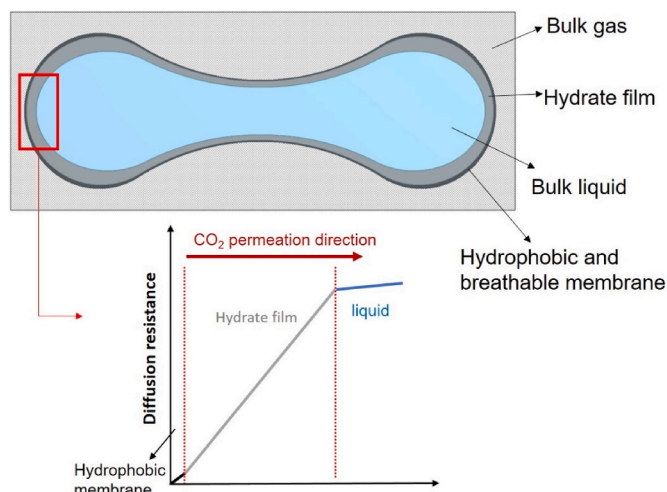


**Fig. 9.** Variation of effective diffusivity of $CO_2$ during hydrate formation for both capsules.



**Fig. 10.** An indicative schematic of the diffusion resistance of different parts of the RBC-shaped capsule as hydrate grows.
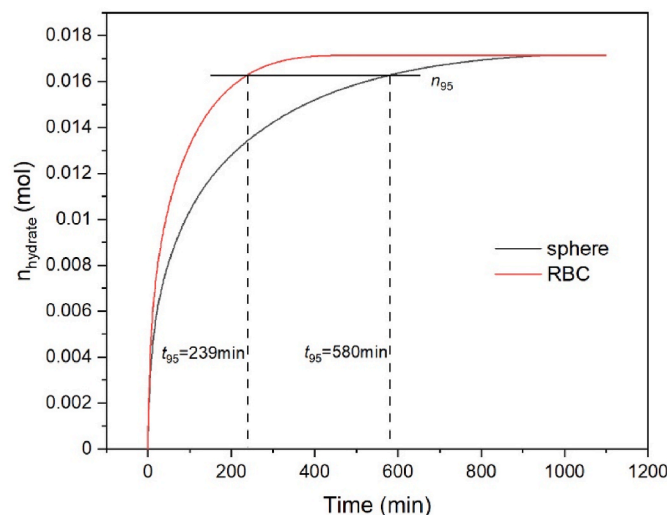


**Fig. 11.** Hydrate formation kinetics for the RBC-shaped and spherical capsules.

which is 58.8% shorter than that of the spherical capsule. The gas uptake efficiency of the RBC is 143% higher than that of the spherical capsule. The average hydrate formation rate per surface area is 0.007285 mol m$^{-2}$ min$^{-1}$ for the spherical capsule and 0.01306 mol m$^{-2}$ min$^{-1}$ for the RBC-shaped capsule. This demonstrates the superiority of RBC-shaped structure in enhancing mass transfer, which is attributed to the large surface area as well as the short diffusion distance of RBC-shaped capsule. In addition, it saves 46.7% and 38.6% of time for RBC and sphere, respectively, when ceasing the reaction at $t_{95}$ rather than reaching the full capacity.

To compare the mass transfer characteristics between the RBC-shaped and spherical capsule during the hydrate formation, the TBAB concentration contours of both capsules at the time of 60, 180 and 300 min are plotted. The TBAB concentration in the capsule decreases, indicating the formation of hydrates. As shown in Table 4, the concentration of TBAB is higher when it is closer to the centre of the capsule, because $CO_2$ first reacts with TBAB at the outer layer of the capsule to form hydrates as $CO_2$ diffuses. After the hydrate at the outer layer is formed, $CO_2$ diffuses through the hydrate layer and reacts with TBAB at the inner part. For the RBC-shaped capsule, hydrate first forms at the concaves and the boundary area of the disc, due to the short diffusion distance at these areas. While for the spherical capsule, hydrate first
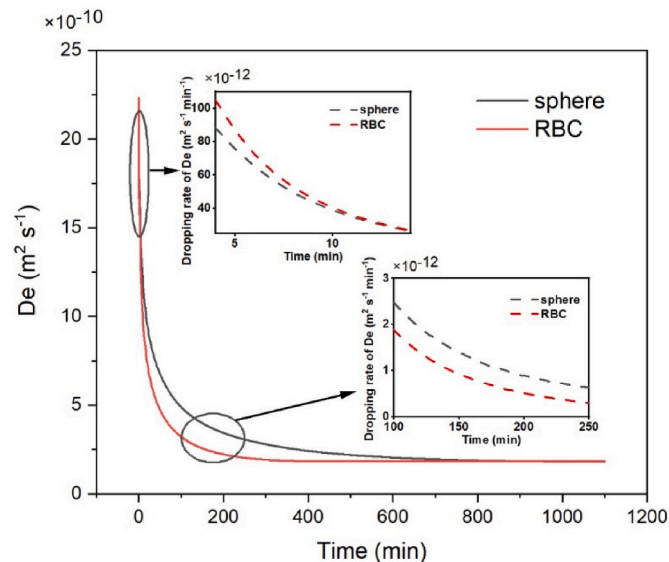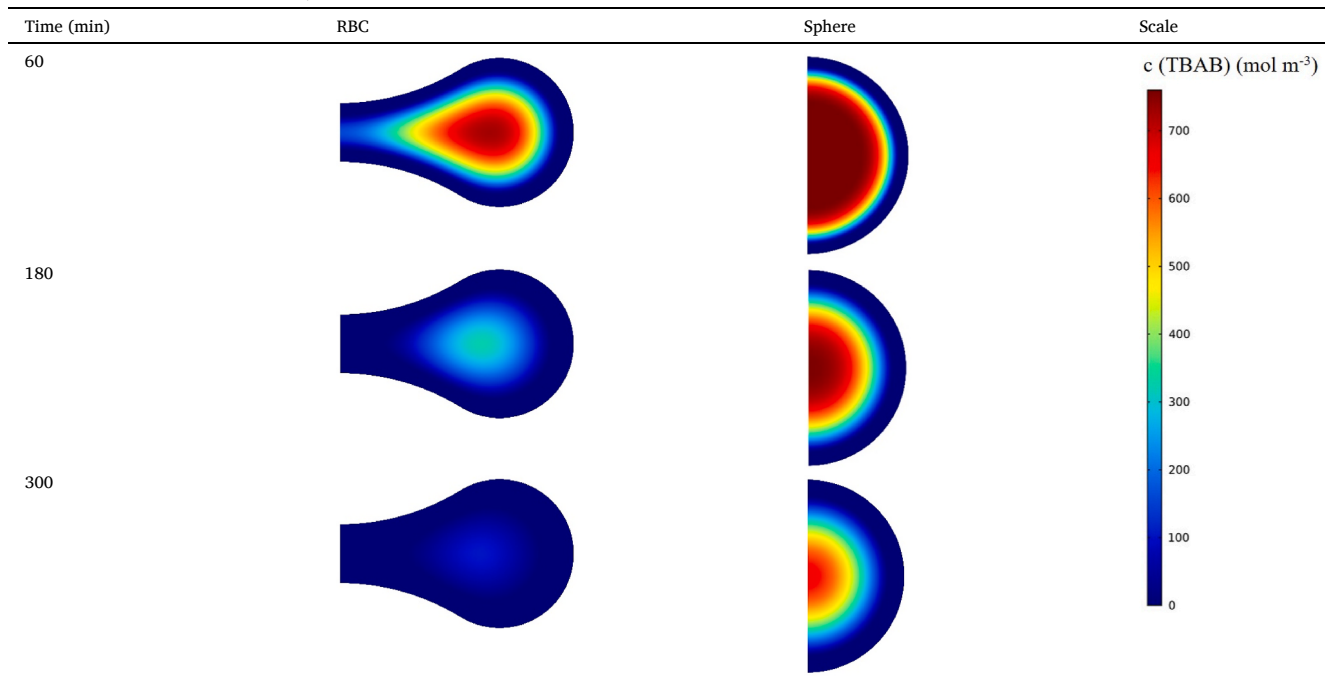
**Table 4**
TBAB concentration contours at 60, 180 and 300 min.

| Time (min) | RBC | Sphere | Scale |
|---|---|---|---|
| 60 | | | c (TBAB) (mol m$^{-3}$) |
| 180 | | | |
| 300 | | | |



forms at the boundary area of the sphere, and grows inwards towards the centre. Since the diffusion distance from boundary to centre is the same in all directions for a sphere, the concentration distribution of hydrate shows a pattern of concentric spheres for the spherical capsule. As is seen from the concentration contours at 300 min, the concentration of TBAB is almost 0 in the RBC-shaped capsule, while it still shows an obvious concentric distribution in the spherical capsule, which justifies the better performance in mass transfer for the RBC structure.

According to the concentration contours of the RBC-shaped capsule, gas diffuses inward from the edge of capsule along the normal direction of the outer surface. Gas hydrate formation is the slowest at the centre of the ring, due to the longest diffusion distance. To better demonstrate the superior mass transfer performance of the RBC-shaped capsule, a normalised diffusion distance (NDD) is defined for the RBC shape as follows:

$$\text{NDD} = \frac{\int z \times dl_1 + r_1 \times l_2}{l_1 + l_2} \qquad (16)$$

where $l_1$ and $l_2$ are the two tangent arcs in half of the rotational symmetry plane as shown in Fig. 12. $z$ is the diffusion distance from the points on $l_1$ to the $x$ axis (always along the normal line of the surface), which varies with the position of the point on $l_1$. For all points on $l_2$, the
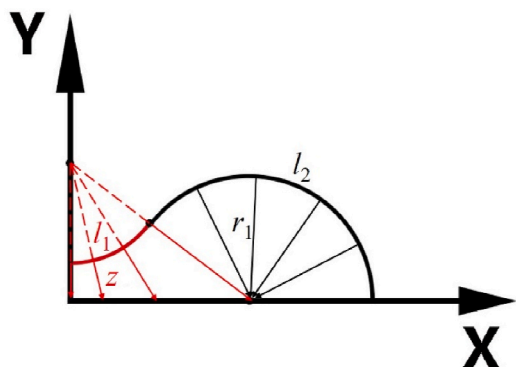
diffusion distances are all equal to $r_1$. At the tangent point of the two arcs, $z$ equals to $r_1$.

For the RBC-shaped capsule considered in this study, the normalised diffusion distance is 6.57 mm, while for the spherical capsule, this value is 17.50 mm (the radius of the sphere). Therefore, the normalised diffusion distance of the RBC is 62.5% shorter than that of the sphere, leading to an earlier completion of hydrate formation.

The temperature contours of both capsules at 60, 180 and 300 min are shown in Table 5. As hydrate formation is an exothermic process, it will lead to a temperature gradient in the capsules. As time goes, the



**Fig. 12.** Schematic of diffusion distance of the RBC-shaped capsule.

**Table 5**
Temperature contours of capsules at 60, 180 and 300 min.

| Time (min) | RBC | Sphere | Scale |
|---|---|---|---|
| 60 | | | T (K) |
| 180 | | | |
| 300 | | | |
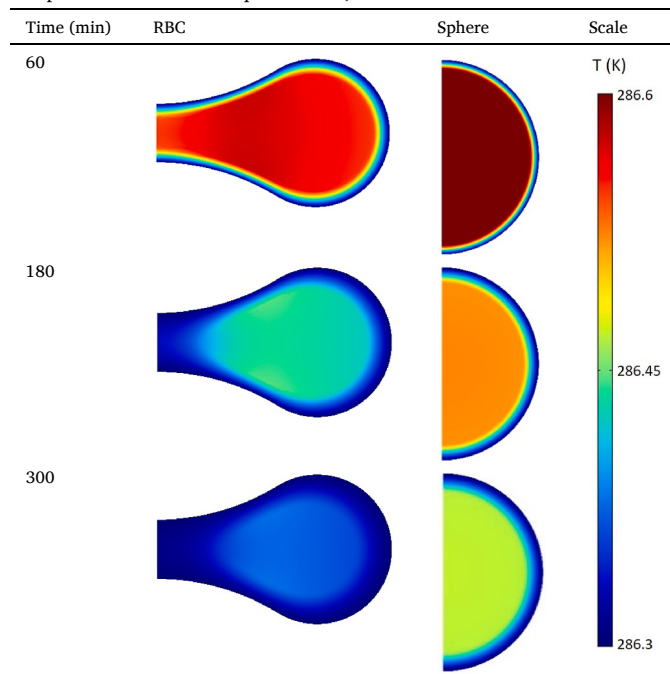
mean temperature in the capsule decreases due to the effective cooling of the water bath, and the temperature gradient also decreases due to the reduced heat releasing rate caused by the decreased hydrate formation rate with time. To some extent, heat transfer in the capsule follows a similar way as the mass transfer. For the RBC-shaped capsule, heat transfer is more efficient at the concaves and the boundary area of the disc, due to shorter heat transfer distance in these areas. For the spherical capsule, heat transfer is in the radial direction from boundary to the inside. Due to the larger surface area, the heat transfer efficiency is much higher in the RBC-shaped capsule, and thus RBC's temperature, especially its inner temperature, goes down more rapidly than that of sphere. Therefore, the RBC structure is not only beneficial for mass transfer, but also for heat transfer.

### 3.2. Effects of initial pressure of $CO_2$

The influence of initial pressure of $CO_2$ on hydrate formation kinetics for both capsules are compared in Fig. 13 (a)-(b). Based on the equation of state of real gas, higher pressure leads to higher concentration, which will increase the concentration gradient on both sides of the membrane and consequently increase the diffusion flux of $CO_2$ through the membrane. As shown in Fig. 13, hydrate formation rate increases with the increase of initial pressure. The values of initial pressure ($p_0$), initial concentration ($c_0$) and $t_{95}$ are listed in Table 6. As $p_0$ increases from 2 to 3 MPa, $t_{95}$ is reduced by 41 min for the RBC-shaped capsule and 95 min for the spherical capsule; and as $p_0$ increases from 3 to 4 MPa, $t_{95}$ is reduced by 32 min for the RBC-shaped capsule and 71 min for the spherical capsule. This indicates $t_{95}$ changes non-linearly with the initial pressure, and the reduction in $t_{95}$ decreases with per unit of pressure increment.

### 3.3. Effects of capsule size

The influence of capsule size on hydrate formation kinetics is investigated for the RBC-shaped capsule. The volume of the model is uniformly scaled to half and double of its original size. The variation of the amount of formed hydrate (mol) over time for the RBC-shaped capsules with the volume of 11.25, 22.5 and 45.0 mL is shown in Fig. 14, and the values of $n_{95}$, $t_{95}$, and the average hydrate formation rate per volume are listed in Table 7. As expected, $t_{95}$ increases with increasing capsule size, but in a non-linear way. According to Fig. 14, hydrate grows faster for a larger capsule size, due to the larger surface area for mass transfer. However, the average hydrate formation rate per volume decreases with increasing size, as observed in Table 7. The reason is that the gas diffusion distance is longer for a larger capsule,

**Table 6**
Influence of $CO_2$ initial pressure (concentration) on $t_{95}$ for both capsules.

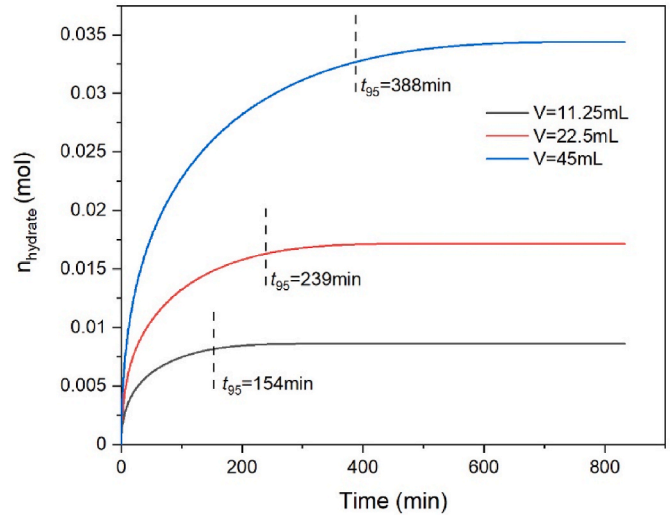| Capsule shape | $p_0$ (MPa) | $c_0$ (mol m$^{-3}$) | $t_{95}$ (min) |
|---|---|---|---|
| RBC | 2 | 950 | 312 |
| | 3 | 1553 | 271 |
| | 4 | 2270 | 239 |
| sphere | 2 | 950 | 746 |
| | 3 | 1553 | 651 |
| | 4 | 2270 | 580 |



**Fig. 14.** Influence of the capsule size on hydrate formation kinetics for the RBC-shaped capsule.
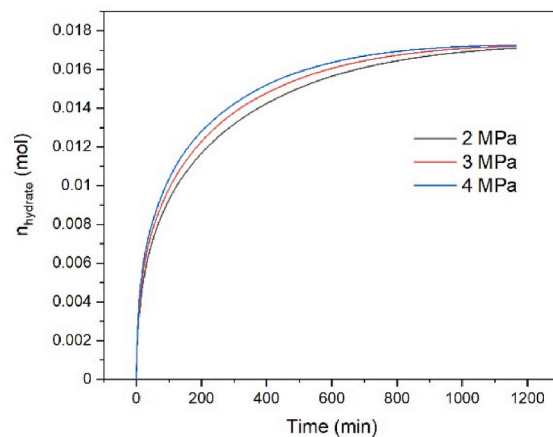
**Table 7**
Key parameters for different capsule sizes for the RBC-shaped capsule.

| Capsule volume (mL) | $n_{95}$ (mol) | $t_{95}$ (min) | Average hydrate formation rate per volume (mol min$^{-1}$ m$^{-3}$) |
|---|---|---|---|
| 11.25 | 0.008161 | 154 | 4.71 |
| 22.5 | 0.01628 | 239 | 3.03 |
| 45 | 0.03268 | 388 | 1.87 |
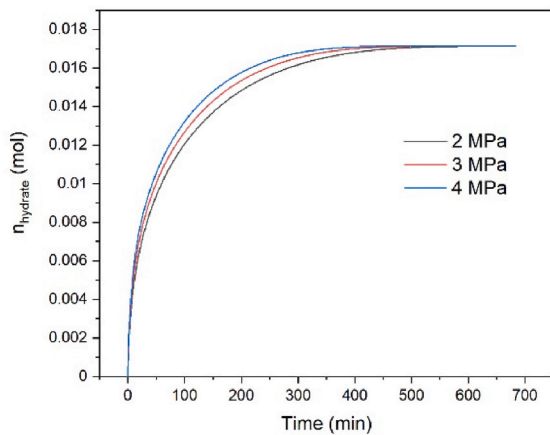


(a) RBC



(b) sphere

**Fig. 13.** Influence of the initial pressure of $CO_2$ on hydrate formation kinetics.

which means $CO_2$ needs to diffuse through a thicker hydrate layer, with a lower effective diffusivity, to react with the unreacted water solution at the core. Therefore, small capsule size is preferred for a higher hydrate formation efficiency, but it doesn't mean a smaller capsule is always better in real engineering applications. On one hand, reducing size will increase the encapsulation difficulty, and on the other, surface-to-volume ratio will increase with decreasing capsule size, leading to higher consumption of membrane and supporting materials for a given amount of gas uptake. Therefore, the selection of capsule size requires comprehensive consideration of factors such as gas uptake efficiency, manufacturing difficulty and cost.
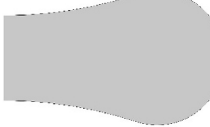
### 3.4. RBC structure optimization

Based on the results and discussions above, the RBC-shaped structure has superior performance in both mass and heat transfer. In practical applications, it is favourable to achieve highest gas uptake efficiency at the lowest possible cost, i.e. lowest consumption of membrane and supporting materials. Therefore, it is necessary to optimise RBC structure to achieve best performance.

The structure of RBC is determined by the four parameters shown in Fig. 2. However, it is unknown how these parameters influence the gas uptake performance of the capsule. The four parameters are constrained by Equation (1). We keep the capsule volume constant and regard the H-to-L ratio as the only variable for comparison. H/L influences the squeezing level at the concaves and the flatness of the capsule. A higher H/L value means a lower squeezing level and higher flatness. The influence of H/L on the hydrate formation kinetics is investigated as we keep L constant as 24.53 mm and the volume of RBC constant as 22.5 mL. Table 8 shows the influence of H/L on the shape of the rotational plane, the surface area, surface-to-volume ratio, $t_{95}$, and the average hydrate formation rate per surface area, and the results are also plotted in Fig. 15. It is found that as the value of H/L increases, the surface-to-volume ratio decreases linearly, while the normalised diffusion distance increases, and the increasing rate decreases. $T_{95}$ is almost unaffected when H/L is between 0.032 and 0.128, then it increases exponentially when it is higher than 0.128. This indicates the RBC structure starts to make significant effect on hydrate formation time when H/L is higher than 0.128. With the decrease of surface area and increase of diffusion distance, the time required to form hydrates increases. As for the average hydrate formation rate per surface area, it first increases linearly with the increase of H/L, then remains almost constant when H/L is between 0.128 and 0.160, and finally decreases with the rise of H/L when it is higher than 0.160. Therefore, the average hydrate formation rate per surface area achieves the maximum value when H/L is between 0.128 and 0.160, which means the RBC-shaped capsule has the best $CO_2$

**Table 8**
Influence of H/L on the RBC structure and hydrate formation kinetics.

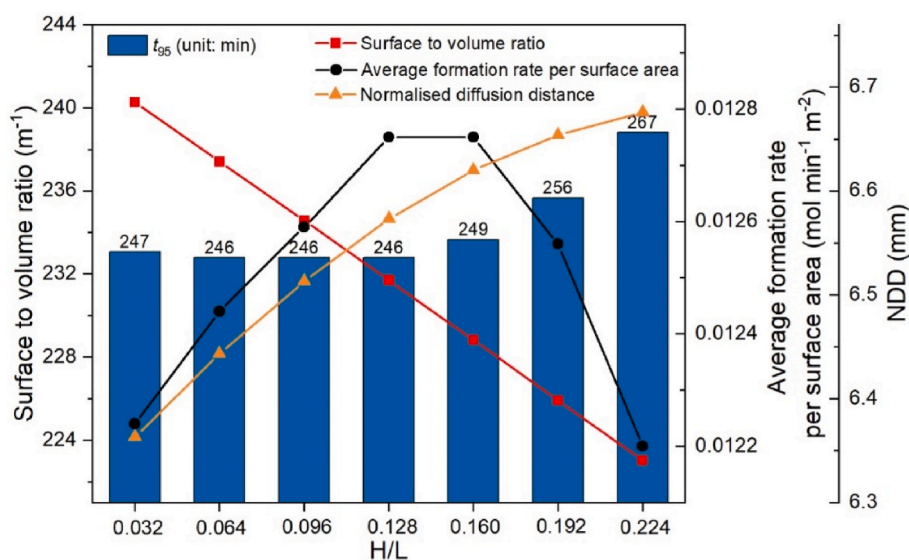| H/L | Rotational plane | S (cm$^2$) | Surface-to-volume ratio (m$^{-1}$) | NDD (mm) | $t_{95}$ (min) | Average hydrate formation rate per surface area (mol min$^{-1}$ m$^{-2}$) |
|---|---|---|---|---|---|---|
| 0.032 | | 54.03 | 240.28 | 6.363 | 247 | 0.01224 |
| 0.064 | | 53.39 | 237.42 | 6.443 | 246 | 0.01244 |
| 0.096 | | 52.75 | 234.57 | 6.513 | 246 | 0.01259 |
| 0.128 | | 52.11 | 231.70 | 6.573 | 246 | 0.01275 |
| 0.16 | | 51.46 | 228.82 | 6.620 | 249 | 0.01275 |
| 0.192 | | 50.81 | 225.92 | 6.654 | 256 | 0.01256 |
| 0.224 | | 50.15 | 223.03 | 6.676 | 267 | 0.01220 |

**Fig. 15.** Influence of H/L on surface-to-volume ratio and hydrate formation kinetics.

uptake performance while using the least membrane material within this range. In real red blood cells of human, the disk diameter is approximately 6.2–8.2 μm, and the minimum thickness in the centre is about 0.8–1 μm [65], which causes the value of H/L in the range of 0.098–0.161. Therefore, the optimised structure of RBC has similar geometrical characteristics as real RBC in human bodies.

## 4. Conclusions

In this paper, based on the principles of biomimetics, a red blood cell (RBC) inspired encapsulation design was proposed to enhance gas-liquid mass transfer and improve $CO_2$ hydrate formation kinetics. A numerical model that integrates mass transfer, heat transfer and intrinsic kinetics was established and experimentally validated. Hydrate formation kinetics was compared between the RBC-shaped and spherical capsule with the same volume, and the effect of initial pressure and capsule size on gas uptake performance was investigated through simulation. A normalised diffusion distance (NDD) is defined for the first time for analysing the shapes of capsule jointly with the surface-to-volume ratio. Finally, the structure of RBC is optimised. The main results conclude that.

(1) Compared to the spherical capsule, $t_{95}$ is reduced by 58.8% and $CO_2$ uptake efficiency is increased by 143% for the RBC-shaped capsule under experiment conditions (4 MPa, 12 °C). RBC-shaped structure has superior performance in both mass transfer and heat transfer.

(2) Hydrate formation rate increases with the increase of initial pressure for both capsules, and $t_{95}$ changes non-linearly with the initial pressure. The reduction rate of $t_{95}$ decreases with the rise of initial pressure. At the same pressure and temperature conditions, $CO_2$ hydrate grows faster for a larger capsule size, but the average hydrate formation rate per volume decreases with the rise of capsule size.

(3) The structure of RBC starts to make significant effect on hydrate formation time when H/L is higher than 0.128. Hydrate formation time increases with the decrease of surface area and increase of NDD. The average hydrate formation rate per surface area achieves the peak (0.01275 mol $min^{-1}$ $m^{-2}$) when H/L is between 0.128 and 0.160 for the RBC structure. This is similar to the geometrical characteristics of real RBCs in human bodies.

This work enables the informed design of HBCC systems with high gas uptake efficiency. Future work will focus on the comprehensive system assessment of an HBCC unit (as shown in Fig. 1 (b)) using multiple RBC inspired capsules.

## Credit author statement

**Yuxuan Zhang:** Investigation, Methodology, Validation, Data Curation, Formal analysis, Writing – original draft. **Xiaoqiang Zhai:** Conceptualization, Methodology, Supervision, Writing – review & editing. **Fengyuan Zhang:** Investigation. **Kamel Hooman:** Supervision, Writing – review & editing. **Hai Zhang:** Supervision. **Xiaolin Wang:** Conceptualization, Resources, Methodology, Supervision, Writing – review & editing.

## Declaration of competing interest

The authors declare that they have no known competing financial interests or personal relationships that could have appeared to influence the work reported in this paper.

## Data availability

Data will be made available on request.

## References

[1] Cao C, et al. A review of CO2 storage in view of safety and cost-effectiveness. Energies 2020;13(3):600.
[2] House KZ, et al. Permanent carbon dioxide storage in deep-sea sediments. Proc Natl Acad Sci USA 2006;103(33):12291–5.
[3] Kang S-P, Lee J-W, Ryu H-J. Phase behavior of methane and carbon dioxide hydrates in meso-and macro-sized porous media. Fluid Phase Equil 2008;274(1–2): 68–72.
[4] Wang X, Dennis M. Thermal energy harvest in the discharge of CO2 semi-clathrate hydrate in an emulated cold storage system. Appl Therm Eng 2017;124:725–33.
[5] Wang X, Zhang F, Lipiński W. Research progress and challenges in hydrate-based carbon dioxide capture applications. Appl Energy 2020;269:114928.
[6] Gholinezhad J, Chapoy A, Tohidi B. Separation and capture of carbon dioxide from CO2/H2 syngas mixture using semi-clathrate hydrates. Chem Eng Res Des 2011;89 (9):1747–51.

[7] Wang S, et al. Measurement of the three-phase (vapour+ liquid+ solid) equilibrium conditions of semi-clathrates formed from mixtures of CO2, CO and H2. J Chem Therm 2013;56:149–52.

[8] Meysel P, et al. Experimental investigation of incipient equilibrium conditions for the formation of semi-clathrate hydrates from quaternary mixtures of (CO2+ N2+ TBAB+ H2O). J Chem Therm 2011;43(10):1475–9.

[9] Babu P, et al. Enhanced kinetics for the clathrate process in a fixed bed reactor in the presence of liquid promoters for pre-combustion carbon dioxide capture. Energy 2014;70:664–73.

[10] Li S, et al. Semiclathrate hydrate phase equilibria for CO2 in the presence of tetra-n-butyl ammonium halide (bromide, chloride, or fluoride). J Chem Eng Data 2010; 55(9):3212–5.

[11] Kim S, Seo Y. Semiclathrate-based CO2 capture from flue gas mixtures: an experimental approach with thermodynamic and Raman spectroscopic analyses. Appl Energy 2015;154:987–94.

[12] Lin W, et al. Thermodynamic properties of semiclathrate hydrates formed from the TBAB+ TBPB+ water and CO2+ TBAB+ TBPB+ water systems. Fluid Phase Equil 2014;372:63–8.

[13] Wang X, Dennis M. Phase equilibrium and formation behaviour of CO2-TBAB semi-clathrate hydrate at low pressures for cold storage air conditioning applications. Chem Eng Sci 2016;155:294–305.

[14] Ding A, et al. Reversible methane storage in porous hydrogel supported clathrates. Chem Eng Sci 2013;96:124–30.

[15] Wang X, Dennis M. Charging performance of a CO2 semi-clathrate hydrate based PCM in a lab-scale cold storage system. Appl Therm Eng 2017;126:762–73.

[16] Zhang F, et al. The effect of sodium dodecyl sulfate and dodecyltrimethylammonium chloride on the kinetics of CO2 hydrate formation in the presence of tetra-n-butyl ammonium bromide for carbon capture applications. Energy 2021;227:120424.

[17] Wang W, et al. Methane storage in dry water gas hydrates. J Am Chem Soc 2008; 130(35):11608–9.

[18] Kwon Y-A, et al. Synthesis of anionic multichain type surfactant and its effect on methane gas hydrate formation. J Ind Eng Chem 2011;17(1):120–4.

[19] Ando N, Kuwabara Y, Mori YH. Surfactant effects on hydrate formation in an unstirred gas/liquid system: an experimental study using methane and micelle-forming surfactants. Chem Eng Sci 2012;73:79–85.

[20] Du J, Li H, Wang L. Effects of ionic surfactants on methane hydrate formation kinetics in a static system. Adv Powder Technol 2014;25(4):1227–33.

[21] Daraboina N, et al. Natural gas hydrate formation and decomposition in the presence of kinetic inhibitors. 2. Stirred reactor experiments. Energy Fuel 2011;25 (10):4384–91.

[22] Kim N-J, et al. Formation enhancement of methane hydrate for natural gas transport and storage. Energy 2010;35(6):2717–22.

[23] Luo Y-T, et al. Study on the kinetics of hydrate formation in a bubble column. Chem Eng Sci 2007;62(4):1000–9.

[24] Adeyemo A. Post combustion capture of carbon dioxide through hydrate formation in silica gel column. University of British Columbia; 2008.

[25] Zhang F, et al. Experimental and numerical study on the kinetics of CO2–N2 clathrate hydrates formation in silica gel column with dodecyltrimethylammonium chloride for effective carbon capture. J Mol Liq 2022:119764.

[26] Yin Z, et al. Numerical analysis of experimental studies of methane hydrate formation in a sandy porous medium. Appl Energy 2018;220:681–704.

[27] Li X-Y, et al. Experimental study of methane hydrate formation and decomposition in the porous medium with different thermal conductivities and grain sizes. Appl Energy 2022;305:117852.

[28] Zhou L, et al. Progress in studies of natural gas storage with wet adsorbents. Energy Fuel 2010;24(7):3789–95.

[29] Fan S, et al. Kinetics and thermal analysis of methane hydrate formation in aluminum foam. Chem Eng Sci 2012;82:185–93.

[30] Mu L, et al. A novel method to improve the gas storage capacity of ZIF-8. J Mater Chem 2012;22(24):12246–52.

[31] Okutani K, Kuwabara Y, Mori YH. Surfactant effects on hydrate formation in an unstirred gas/liquid system: an experimental study using methane and sodium alkyl sulfates. Chem Eng Sci 2008;63(1):183–94.

[32] Shi B-H, Fan S-S, Lou X. Application of the shrinking-core model to the kinetics of repeated formation of methane hydrates in a system of mixed dry-water and porous hydrogel particulates. Chem Eng Sci 2014;109:315–25.

[33] Cheng X, Zhai X. Thermal performance analysis of a novel PCM capsule in red blood cell shape. Appl Therm Eng 2017;120:130–7.

[34] Cheng X, et al. Numerical study of forced convection over phase change material capsules in a traditional spherical shape and a biomimetic shape. J Energy Storage 2020;31:101526.

[35] Wang X, et al. Experimental evaluation of heat transfer performance under natural and forced convection around a phase change material encapsulated in various shapes. Sustain Energy Technol Assessments 2021;44:101025.

[36] Yin Z, et al. A review of gas hydrate growth kinetic models. Chem Eng J 2018;342: 9–29.

[37] Englezos P, et al. Kinetics of formation of methane and ethane gas hydrates. Chem Eng Sci 1987;42(11):2647–58.

[38] Clarke MA, Bishnoi P. Determination of the intrinsic kinetics of CO2 gas hydrate formation using in situ particle size analysis. Chem Eng Sci 2005;60(3):695–709.

[39] Mohammadi A, et al. Kinetic study of carbon dioxide hydrate formation in presence of silver nanoparticles and SDS. Chem Eng J 2014;237:387–95.

[40] Daimaru T, Yamasaki A, Yanagisawa Y. Effect of surfactant carbon chain length on hydrate formation kinetics. J Petrol Sci Eng 2007;56(1–3):89–96.

[41] Fan S, et al. Efficient capture of CO2 from simulated flue gas by formation of TBAB or TBAF semiclathrate hydrates. Energy Fuel 2009;23(8):4202–8.

[42] Feyzi V, Mohebbi V. Experimental study and modeling of the kinetics of carbon-dioxide hydrate formation and dissociation: a mass transfer limited kinetic approach. J Nat Gas Sci Eng 2020;77:103273.

[43] Herri J-M, et al. Methane hydrate crystallization mechanism from in-situ particle sizing. AIChE J 1999;45(3):590–602.

[44] Turner DJ, Miller KT, Sloan ED. Methane hydrate formation and an inward growing shell model in water-in-oil dispersions. Chem Eng Sci 2009;64(18): 3996–4004.

[45] Yang D, et al. Kinetics of CO2 hydrate formation in a continuous flow reactor. Chem Eng J 2011;172(1):144–57.

[46] Shindo Y, et al. Kinetics of formation of CO2 hydrate. Energy Convers Manag 1993; 34(9–11):1073–9.

[47] Uchida T, et al. CO2 hydrate film formation at the boundary between CO2 and water: effects of temperature, pressure and additives on the formation rate. J Cryst Growth 2002;237:383–7.

[48] Shindo Y, et al. Kinetics of the formation of CO2 hydrate on the surface of liquid CO2 droplet in water. Energy Convers Manag 1996;37(4):485–9.

[49] Teng H, Kinoshita C, Masutani S. Hydrate formation on the surface of a CO2 droplet in high-pressure, low-temperature water. Chem Eng Sci 1995;50(4): 559–64.

[50] Dalmazzone D, Hamed N, Dalmazzone C. DSC measurements and modelling of the kinetics of methane hydrate formation in water-in-oil emulsion. Chem Eng Sci 2009;64(9):2020–6.

[51] Liang S, et al. Molecular mechanisms of gas diffusion in CO2 hydrates. J Phys Chem C 2016;120(30):16298–304.

[52] Shi B-H, et al. An inward and outward natural gas hydrates growth shell model considering intrinsic kinetics, mass and heat transfer. Chem Eng J 2011;171(3): 1308–16.

[53] Pan L, et al. Super-resolution microscopy reveals the native ultrastructure of the erythrocyte cytoskeleton. Cell Rep 2018;22(5):1151–8.

[54] Feng S, et al. Progress and perspectives in PTFE membrane: preparation, modification, and applications. J Membr Sci 2018;549:332–49.

[55] matweb.com.

[56] Hashemi H, et al. State of the art and kinetics of refrigerant hydrate formation. Int J Refrig 2019;98:410–27.

[57] Fujiura K, et al. Thermal conductivity measurements of semiclathrate hydrates and aqueous solutions of tetrabutylammonium bromide (TBAB) and tetrabutylammonium chloride (TBAC) by the transient hot-wire using parylene-coated probe. Fluid Phase Equil 2016;413:129–36.

[58] dielectricmfg.com.

[59] Asaoka T, Kumano H, Serita M. Measurement of latent heat of tetra-n-butylammonium bromide (TBAB) hydrate. Int J Refrig 2013;36(3):992–7.

[60] Lin W, et al. Thermodynamic studies of CO2-TBAB-water system. In: 7th international conference on gas hydrates, vol. 2011. ICGH; 2011.

[61] Zhang F, et al. Experimental and numerical analysis of CO2 and CH4 hydrate formation kinetics in microparticles: a comparative study based on shrinking core model. Chem Eng J 2022:137247.

[62] Wang X, Dennis M. Influencing factors on the energy saving performance of battery storage and phase change cold storage in a PV cooling system. Energy Build 2015; 107:84–92.

[63] Sebők B, et al. Diffusivity, permeability and solubility of H2, Ar, N2, and CO2 in poly (tetrafluoroethylene) between room temperature and 180 C. Polym Test 2016; 49:66–72.

[64] Ranganathan A. The levenberg-marquardt algorithm. Tutorial on LM algorithm 2004;11(1):101–10.

[65] Turgeon ML. Clinical hematology: theory and procedures. Lippincott Williams & Wilkins; 2005.